Ultrafast laser one-step construction of 3D micro-/nanostructures achieving high-performance zinc metal anodes

Yanan Liu[1†], Ye Ding[2†], Zeping Liu[3], Xingchen Li[4], Sichao Tian[5*], Lishuang Fan[3*], Jichang Xie[6], Liangliang Xu[7], Jinwoo Lee[7*], Jian Li[8] and Lijun Yang[1*]

[†]Yanan Liu and Ye Ding are contributed equally to this work.

*Correspondence:
tiansichao@outlook.com;
fanlsh@hit.edu.cn; jwlee1@kaist.
ac.kr; yljtj@hit.edu.cn

[1] Zhengzhou Research Institute, Harbin Institute of Technology, Zhengzhou 450000, P. R. China
[2] Suzhou Research Institute, Harbin Institute of Technology, Suzhou 215104, P. R. China
[3] School of Chemistry and Chemical Engineering, Harbin Institute of Technology, Harbin 150001, P. R. China
[4] Defense Innovation Institute, Chinese Academy of Military Science, Beijing 100071, P. R. China
[5] Institute of Medicinal Plant Development, Chinese Academy of Medical Sciences and Peking Union Medical College, Beijing 100193, P. R. China
[6] Laboratoire Roberval, UTC, Sorbonne Universités, Université de Technologie de Compiègne, Centre de recherche Royallieu, CS60319, 60203 Compiègne Cedex, France
[7] Department of Chemical and Biomolecular Engineering, Korea Advanced Institute of Science and Technology (KAIST), Daejeon 34141, Republic of Korea
[8] School of Mechanical Engineering, Beijing Institute of Technology, Beijing 100081, P. R. China

Abstract

Aqueous zinc-ion batteries provide a most promising alternative to the existing lithium-ion batteries due to their high theoretical capacity, intrinsic safety, and low cost. However, commercializing aqueous zinc-ion batteries suffer from dendritic growth and side reactions on the surface of metallic zinc, resulting in poor reversibility. To overcome this critical challenge, here, we report a one-step ultrafast laser processing method for fabricating three-dimensional micro-/nanostructures on zinc anodes to optimize zinc nucleation and deposition processes. It is demonstrated that the three-dimensional micro-/nanostructure with increased specific surface area significantly reduces nucleation overpotential, as well as preferentially absorbs zinc ions to prevent dendritic protuberances and corrosion. As a result, the presence of three-dimensional micro-/nanostructures on the zinc metal delivers stable zinc plating/stripping beyond 2500 h (2 mA cm^{-2}/1 mAh cm^{-2}) in symmetric cells, a high Coulombic efficiency (99.71%) in half cells, and moreover an improved capacity retention (71.8%) is also observed in full cells. Equally intriguingly, the pouch cell with three-dimensional micro-/nanostructures can operate across various bending states without severely compromising performance. This work provides an effective strategy to construct ultrafine and high-precision three-dimensional micro-/nanostructures achieving high-performance zinc metal anodes and is expected to be of immediate benefit to other metal-based electrodes.

Keywords: Ultrafast laser processing, One-step manufacturing, Zinc metal anode, Three-dimensional micro-/nanostructures, Dendrite-free

Introduction

The intrinsic safety and high ionic conductivity of aqueous electrolytes have pushed aqueous zinc-ion batteries (AZIBs) to the forefront [1–3], which are expected as the next generation of convenient energy storage systems beyond lithium-ion batteries due to the advantages of high safety, environmental friendliness, and natural abundance [4–6]. In view of outstanding features in low electrochemical potential (-0.76 V vs. standard hydrogen electrode), high theoretical weight and volume capacity (820 mAh g^{-1} and 5855 mAh cm^{-3}), metallic zinc (Zn) foil has become a promising and common anode

material for AZIBs [7]. Additionally, the non-toxic Zn anode has high stability in the air, remarkably improving the convenient fabrication and safety of practical AZIBs. However, the uncontrollable dendrite growth, unwanted side reactions/corrosions, and poor plating/stripping reversibility of Zn anodes substantially shorten the device performance and become an obstacle for applications of AZIBs [8, 9].

Towards this end, considerable research efforts have been proposed to improve the performance of Zn anodes, including electrolyte optimization [10–12], Zn alloying [13–15], protective layers [16–18], and three-dimensional micro-/nanostructures (3DMNs) [19–22]. However, the increased costs of electrolyte compositions and the poor adhesion of the protective layer make it challenging to maintain a stable repeat Zn plating/stripping process at high-performance levels. From the perspective of structure fabrication strategy, 3DMNs can provide more electrochemical active sites, significantly reducing the local current density. Therefore, constructing 3DMNs on Zn anodes provides an effective way to regulate the deposition kinetics of Zn^{2+} and suppress dendrite growth [23]. However, the complex manufacturing process and costly issues of 3DMNs severely hamper the preparation of high-performance Zn anodes. More immediately, regulating 3DMNs at the nano or even micro dimension remains challenging. Meanwhile, pre-treatment (mechanical/electrochemical polishing) and post-treatment (protective coatings and heat treatment) on Zn foils are required to achieve satisfactory capacity storage performance in most modification strategies [24–27]. Nevertheless, the low hardness and melting point of metallic Zn foils increase the steps and difficulty of surface treatment, thus largely impeding the practical 3DMNs.Therefore, it is essential to establish a simple and one-step approach for preparing ultrafine and controllable 3DMNs on commercial Zn foils to suppress dendrite growth and improve the cycling stability of AZIBs.

As a typical one-step processing method, ultrafast laser processing technology (ULPT) benefits from high efficiency, excellent repeatability, maskless, and high controllability, which offers that for a diverse range of applications in manufacturing micro- and nanostructures [28]. The ability of ultrafast lasers to concentrate energy within a time interval of picoseconds to femtoseconds allows the laser beam to focus on ultrafine spatial regions, making it to be suitable for processing micro-/nanostructures with low melting points/hardness and flexible materials [29]. The high-power density of ultrafast lasers is sufficient to peel off the outer electrons of the material, enabling surface ablation before energy diffusion to achieve unique "cold processing," which is able to considerably enhance processing accuracy and irreversible damage (such as deformation and microcracks). With the development of microelectronic devices towards precision, miniaturization, and flexibility, ULPT has emerged in the field of micro-/nanomanufacturing, effectively modifying material properties, including surface wettability [30], surface coloring [31], optical properties [32], hardness [33], and friction and wear characteristics [34]. Furthermore, the ultrahigh flexibility and controllability of ULPT suggest that it is suited for preparing various energy storage and sensing devices, such as water micro batteries [35], lithium-ion batteries [36], supercapacitors [37–40], and photodetectors [41].

Different from previous reports, herein, a one-step ULPT is utilized to prepare superfine and high-precision 3DMNs on Zn metal anodes for the sake of optimizing Zn plating/stripping behavior and cycling stability. The current method aims to achieve one-step
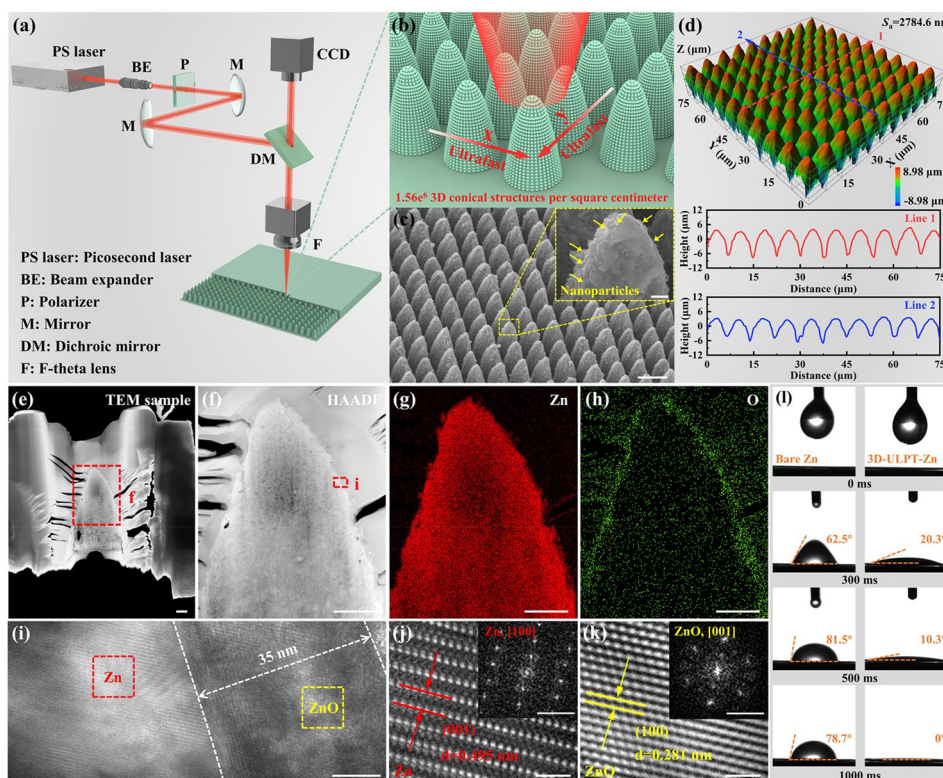
Fig. 1 **a**-**b** Schematic illustration of the 3DMN prepared by the one-step ULPT. **c** SEM and **d** 3D images of the 3DMN. **e** TEM sample fabricated by the standard focused ion beam. **f** High angle annular darkfield (HAADF) image. EDS-mapping results of elements (**g**) Zn and (**h**) O. **i** HRTEM image of Zn/ZnO interface. HRTEM images of (**j**) Zn and (**k**) ZnO. The insets show corresponding SAED patterns of Zn[100] and ZnO[001]. **l** Contact angles of 2 M ZnSO$_4$ aqueous electrolyte on the bare Zn and 3D-ULPT-Zn anodes. Scale bar: 10 μm for c (1 μm for the inset), 1 μm for e-h, 10 nm for i, and 1 nm for j-k (5 1/nm for the insets)

and controllable preparation of 3DMNs on Zn anodes, which avoids complicated procedures, including polishing/protective coating and heat treatment, thus significantly simplifying the manufacture of AZIBs. Additionally, most of the reported modified Zn anodes require assistance in fine-tuning the size and morphology of 3DMNs, especially at the micro-/nanoscale, which results in inadequately exploiting the benefits of 3DMNs. In the present study, the one-step ULPT well resolves these issues. The hydrophilic and zincophilic 3DMNs help to increase the flux of Zn ions on the electrode, thus improving the feasibility of Zn deposition. Furthermore, the in situ generated Zn/ZnO layer effectively prevents the accumulation of by-products to significantly enhance cycling stability. This strategy offers a simple and brand-new method for constructing 3DMNs to achieve high-performance Zn anodes and advancing the practical application of AZIBs.

Results and discussion

In the present study, the 3DMN was prepared on the Zn anode by one-step ULPT (Fig. 1a) in the atmospheric environment. The morphology of the 3DMN is controlled by the number of scanning repetitions (R_s), with values of 1, 5, 10, 20, 30, and 40 (the laser-treated Zn anode is labeled as "3D-ULPT-Zn-R_s"). The effect of parameter R_s on the morphology evolution of 3DMNs is provided in Fig. S1 (Supporting Information),

indicating that R_s=20 leads to the complete formation of 3DMNs on the Zn anode. The orderly arrangement and consistency of 3DMNs can be seen from enlarged scanning electron microscope (SEM) images, verifying the high precision characteristics of the one-step ULPT. Furthermore, the 3DMN contains up to $1.56e^6$ 3D conical structures per square centimeter (Fig. 1b), remarkably increasing the specific surface area and contributing more electrochemical reaction sites. Notably, a single laser scan (R_s=1) can remove the rough and irregular surface of the commercial Zn foil, leading to the formation of periodic micro-/nanostructures. Meanwhile, the depth of the 3DMN increases with the R_s value (Fig. S2, Supporting Information). Based on the SEM image (Fig. 1c), it is seen that the micron-sized 3D array is composed of periodic conical structures with a nanosized surface substructure. The nanoparticles were identified as ZnO (Fig. S3, Supporting Information), further increasing the specific surface area of 3DMNs. The 3D image (Fig. 1d) indicates that the overall height of the 3DMN is about 11 μm with a spacing of 8 μm, in agreement with the laser scanning spacing. Combined with the optimization results of macroscopic morphology (Fig. S4, Supporting Information) and galvanostatic charge-discharge (GCD) performance (Fig. S5, Supporting Information), the 3D-ULPT-Zn-20 (for simplicity, it is defined as 3D-ULPT-Zn) exhibits the best cycling performance. In comparison, the cusp effect caused by rough surfaces and irregular protrusions of the bare Zn (Figs. S6-S7, Supporting Information) provides a fitting site for dendritic growth.

Under ultrafast laser processing, the irradiated Zn region is ejected from the material under high temperature and pressure. It is solidified and deposited on the conical structure surface through ultrafast solidification to form a 3DMN. Furthermore, the non-contact processing characteristic of the ULPT improves the accuracy and quality of processing. Due to processing executed under atmospheric conditions, the presence of moisture leads to the formation of an oxide layer. However, because of the ultrafast solidification characteristics of laser processing, a relatively thin oxide layer is expected to generate on the surface of the 3DMN, which is supported by the fact that no structural information except Zn metal can be found in the X-ray diffraction (XRD) patterns (Fig. S8, Supporting Information). Therefore, the standard focused ion beam technique was performed to determine the phase structure of the 3DMN (Fig. 1e). The energy dispersive spectroscopy (EDS) mapping results within the red box i (Fig. 1f) reveal that the element O (Fig. 1h) is distributed on the 3DMN surface. Further observation via high-resolution transmission electron microscopy (HRTEM) indicated that the ZnO layer tightly adhered to the Zn surface with a thickness of approximately 35 nm (Fig. 1i). In addition, HRTEM images (Fig. 1j-k) and corresponding selected area electron diffraction (SAED) patterns can be well indexed in the Zn[100] and ZnO[001] zone axis, indicating a unique Zn(001)/ZnO(100) interface formed. The electrode/electrolyte interface contact can be quantitatively evaluated by analyzing the contact angle between the electrode and the aqueous electrolyte. Fig. 1(l) illustrates that the contact angle of the 3D-ULPT-Zn anode with the electrolyte (0°) is significantly lower than that of bare Zn (78.7°), indicating excellent hydrophilicity. Such a result means that the 3DMNs can allow homogeneous Zn^{2+} distribution to enhance the feasibility of deposition. All these characterizations verified the 3DMN was successfully manufactured on Zn anodes,

which is expected to accelerate the deposition and transfer kinetics of Zn for achieving dendrite-free and ultrastable Zn metal anodes.

The 3D-ULPT-Zn anode prepared by the one-step ULPT is employed for AZIBs. The ex-situ SEM observation revealed the nucleation and growth behaviors of Zn electrodes. As shown in Fig. 2(a), due to the irregular surface energy caused by the rough Zn, apparent dendrites were observed after 3 mAh cm^{-2} and continuously aggregated after 6 mAh cm^{-2} (Fig. 2b). Additionally, protrusions appeared (Fig. 2c) when the deposition capacity was increased to 9 mAh cm^{-2}, which could result in reduced cell performance, even an internal short circuit. Fig. 2(c-d) shows cracks in the bare Zn anode after 9 mAh cm^{-2} and 12 mAh cm^{-2}. According to the previous study, the rough surface of the bare Zn exhibits the ability to induce uneven Zn distribution, resulting in disordered stress on the electrode surface [42, 43]. The accumulated internal stress triggered by continuous deposition cannot be released and will eventually cause the formation of dendrites and electrode cracking. In contrast, the 3D-ULPT-Zn anode exhibits minor morphological alterations after plating for 3 mAh cm^{-2}. Zn is almost entirely deposited on the conical surface, exhibiting homogeneously distributed reduced-size nanosheet structures rather than dendrites. The optimized deposition could be attributed to the increased specific
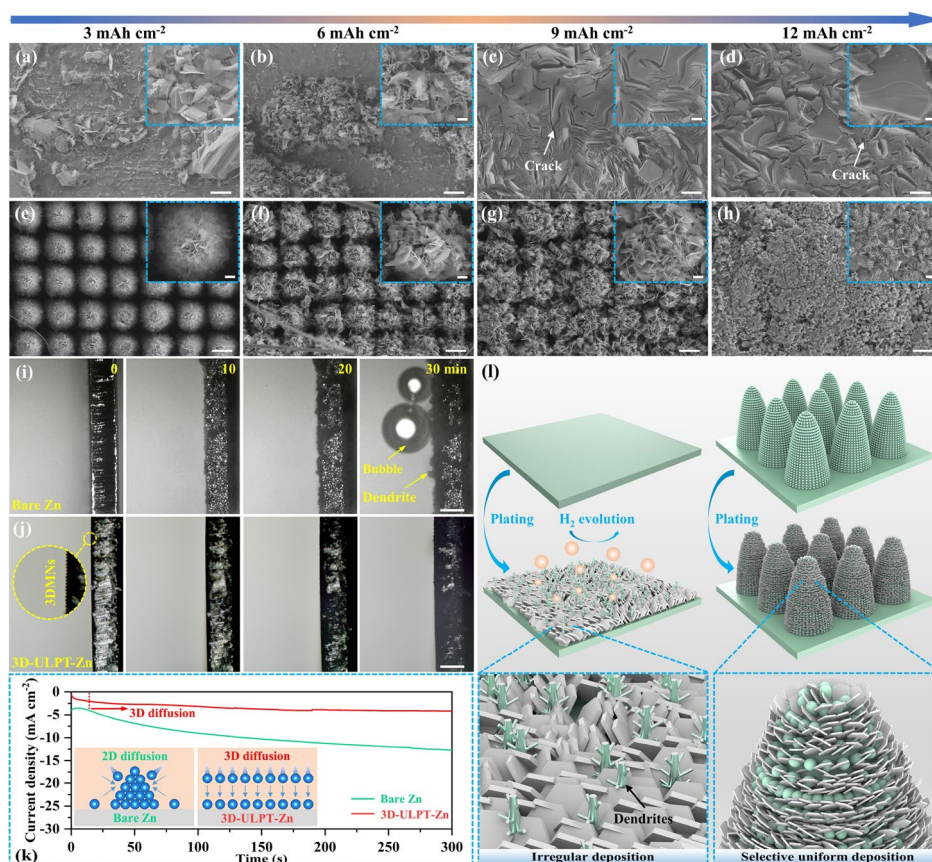
Fig. 2 SEM images of (**a**-**d**) bare Zn and (**e**-**h**) 3D-ULPT-Zn anodes deposited at various areal capacities with a fixed current density of 5 mA cm^{-2}. In situ optical microscopy visualization of Zn deposited on (**i**) bare Zn and (**j**) 3D-ULPT-Zn anodes. **k** The current-time (*i-t*) curves of bare Zn and 3D-ULPT-Zn anodes at an overpotential of -150 mV. **l** Schematic illustration of the Zn deposition process in bare Zn and 3D-ULPT-Zn anodes. Scale bar: 5 μm for a-h (1 μm for the insets) and 100 μm for i-j

surface area of the conical structure combined with ZnO nanoparticles and the stronger adsorption of Zn^{2+} by the Zn/ZnO layer (validated by subsequent simulation calculations). As the capacity increases, Zn deposition gradually diffuses into the gaps between the conical structure (Fig. 2e-h). As the capacity increased to 12 mAh cm^{-2}, the gap was filled thoroughly, and a dense and dendrite-free morphology was maintained. To highlight the advantages of 3DMNs, consistent deposition tests were performed on mechanically polished Zn foils (Fig. S10, supporting information). As shown in Fig. S11, a flat Zn surface can effectively alleviate the "tip effect" at low capacity (3 mAh cm^{-2}). However, the rough deposition morphology is still maintained at high capacity (Fig. S11d). As a comparison, the 3D images (Fig. S12, Supporting Information) at the areal capacity of 12 mAh cm^{-2} confirm that the 3DMNs induce dense and uniform deposition. In addition, EDS analysis (Fig. S13, Supporting Information) of different electrodes at 5 mA cm^{-2} and 12 mAh cm^{-2} verified the optimal suppression performance of 3D-ULPT-Zn anodes (with lower O and S element contents) on side reactions.

The morphology evolution of the Zn plating process was visualized through in situ optical microscopy testing (Fig. S14, Supporting Information) to further prove that the 3D-ULPT-Zn anode is able to induce uniform Zn deposition and inhibit the formation of dendrites. Fig. 2(i) shows that spots randomly appeared upon the bare Zn anode after 10 min, and the Zn deposition became uneven after 20 min. Finally, mossy aggregation and dendrites can be observed after 30 min, which is attributed to the self-amplification behavior triggered by the rapid development of protrusions. Besides, the generation of bubbles can interfere with the plating process, which could lead to internal short-circuiting and low Coulombic efficiency (CE). However, the 3D-ULPT-Zn anode exhibits a dense and smooth surface throughout the plating process (Fig. 2j). The current-time (*i-t*) curve is performed to reveal differences in the Zn deposition behavior of electrodes, and current changes can serve as sensitive signals for Zn nucleation process and surface change. As shown in Fig. 2(k), the current density of the bare Zn anode maintained increasing within 300 s, indicating an uncontrolled 2D diffusion process and severe dendritic growth attributed to the infamous "tip effect". On the contrary, due to the significantly increased specific surface area of micro-cones and anti-corrosive Zn/ZnO layer, the 3D-ULPT-Zn anode exhibited a fast constant current density (2.1 mA cm^{-2}) after a transient current density increase (13 s), reflecting a stable 3D diffusion process in the subsequent deposition process, where uneven Zn deposition was prominently impeded. During the Zn plating process (insets in Fig. 2k), Zn^{2+} is first reduced to Zn, and then adsorbs onto active sites of 3DMNs, restricting 2D diffusion on the electrode surface and facilitating uniform Zn deposition. Such a satisfactory result reveals that the 3DMN can optimize the Zn deposition process and restrain the lateral diffusion and aggregation of Zn^{2+}, thereby inhibiting dendrite growth.

The side reaction is closely related to the generation of $Zn_4SO_4(OH)_6 \cdot xH_2O$ and the occurrence of hydrogen evolution reaction (HER) [44]. Along this line, Tafel plots comparison (Fig. S15, Supporting Information) indicates that the corrosion current density (I_{corr}) of the 3D-ULPT-Zn anode (0.942 mA cm^{-2}) is significantly lower than that of bare Zn (1.728 mA cm^{-2}). Convincingly, the morphology of the 3D-ULPT-Zn anode (Fig. S16, Supporting Information) delivered a smooth and uniform surface after immersing in the 2 M $ZnSO_4$ aqueous electrolyte for 5 days, while the surface of bare Zn exhibited

cracks and corrosion pits. In combination with the XRD patterns (Fig. S17, Supporting Information), the significantly reduced intensity of by-products signifies a superior corrosion resistance of the 3D-ULPT-Zn anode. Furthermore, the linear scanning voltammetry (LSV) curves (Fig. S18, Supporting Information) indicate that the initial potential of the 3D-ULPT-Zn anode (-1.84 V vs. Ag/AgCl) is obviously lower than that of the bare Zn (-1.75 V vs. Ag/AgCl). The sizeable negative shift means that the 3DMN can act as a barrier to prevent the decomposition of the aqueous electrolyte interface. Besides, SEM images (Fig. S19, Supporting Information) show the uniform deposition and dendrite-free topography that occurred on the 3D-ULPT-Zn anode after different cycles. As expected, the negligible strength intensity of by-products (Fig. S20, Supporting Information) indicates enhanced side reaction resistance of the 3D-ULPT-Zn anode. The aforesaid results confirm that the unsatisfactory side reactions have been significantly suppressed by the constructed 3D-ULPT-Zn anode. Fig. 2(l) presents a schematic diagram to elucidate the Zn deposition process on bare Zn and 3D-ULPT-Zn electrodes. The uneven deposition behavior on the bare Zn anode leads to the growth of dendrites, accompanied by severe HER, which raises the risk of short circuits. In contrast, the super-hydrophilic 3D-ULPT-Zn anode with ideal spatial selective deposition behavior effectively improves cycling stability and inhibits detrimental side reactions. More importantly, uniform deposition at high capacity provides a reliable route to construct high-performance Zn anodes.

Benefiting from the optimized Zn deposition behavior and enhanced side reaction resistance, the 3D-ULPT-Zn anode is anticipated to provide ultrastable cycling stability for AZIBs. As expected, the 3D-ULPT-Zn anode exhibits ultralow nucleation overpotential at varied current densities and areal capacities compared to the bare Zn electrode (Fig. S21, Supporting Information). The difference in voltage drop demonstrates that the 3DMN effectively reduces the energy barrier for Zn nucleation, which is beneficial for inhibiting dendrite growth. Fig. 3(a) illustrates that the Zn//Zn cell produces a voltage hysteresis of 72.6 mV at a current density of 2 mA cm^{-2} and an areal capacity of 1 mAh cm^{-2}. It exhibited an abnormal voltage curve at 351 h, indicating that dendrites penetrated the separator and caused the battery failure. Excitingly, the 3D-ULPT-Zn//3D-ULPT-Zn cell maintains a low overpotential (23.1 mV) and stable cyclic performance for 2530 h (Figs. 3a and S22, Supporting Information), which benefits from the enhanced Zn^{2+} transport. The insets exhibit classic cycling curves that can eliminate the illusion of stable cycling caused by short-circuiting and "soft short-circuiting" [45]. Even under a harsher test condition (15 mA cm^{-2} and 1 mAh cm^{-2}), the 3D-ULPT-Zn//3D-ULPT-Zn cell still operated for 500 h (Fig. 3b) with low voltage hysteresis (83 mV) and flat voltage plateau, demonstrating its excellent cycling performance at high current density. However, due to the severe uneven Zn deposition, the abnormal voltage-time curve and subsequent weak voltage response of the Zn anode after 18.2 h indicated that dendrites penetrated the separator and caused a short circuit. Compared to the bare Zn, the durability of 3D-ULPT-Zn anode can be certified by a noticeable improvement in the high current density of 15 mA cm^{-2} and an areal capacity of 15 mAh cm^{-2} (Fig. 3c). In particular, the Zn//Zn cell exhibited unstable voltage fluctuations after 27 h, while the 3D-ULPT-Zn//3D-ULPT-Zn cell maintained a lower and stable polarization voltage until 240 h. Furthermore, the by-product intensity (Fig.
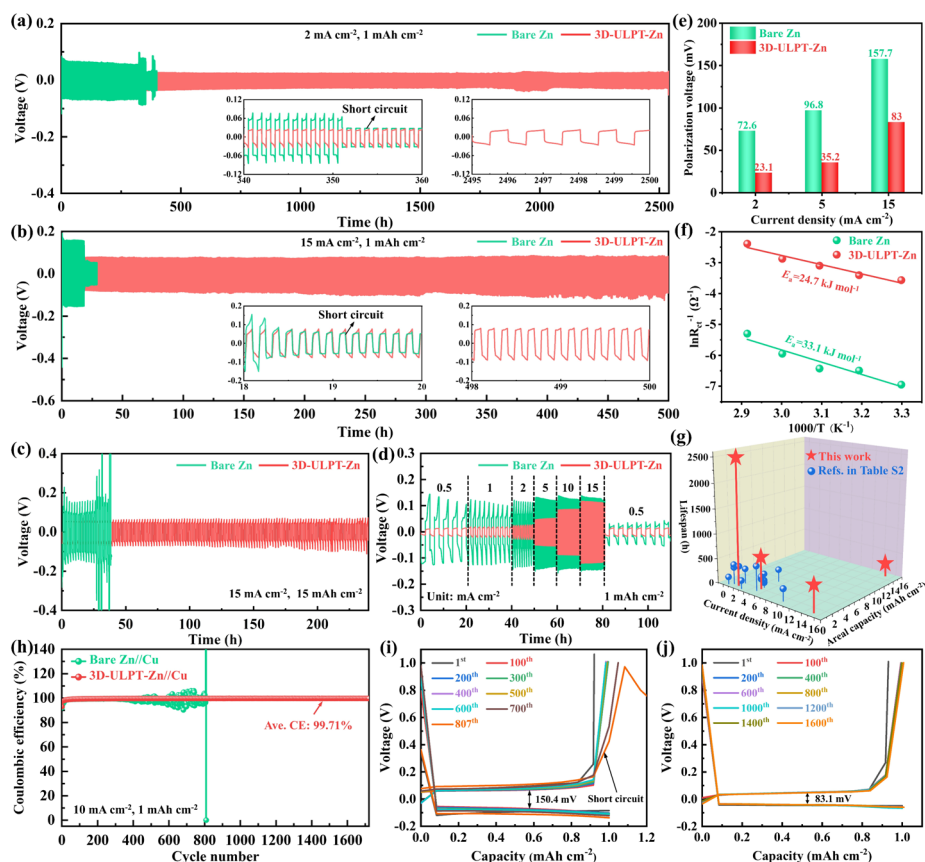
Fig. 3 Electrochemical performance of different electrodes. GCD curves of Zn//Zn and 3D-ULPT-Zn//3D-ULPT-Zn symmetric cells at different current densities and capacities: (**a**) 2 mA cm^{-2}, 1 mAh cm^{-2}, (**b**) 15 mA cm^{-2}, 1 mAh cm^{-2}, (**c**) 15 mA cm^{-2}, 15 mAh cm^{-2}. **d** Rate performance. **e** Polarization voltages of bare Zn and 3D-ULPT-Zn anodes under different current densities with a fixed areal capacity of 1 mAh cm^{-2}. **f** Arrhenius curves and comparison in E_a of bare Zn and 3D-ULPT-Zn anodes. **g** The lifespan comparison between this work and the previously reported 3D structure construction methods. **h** CEs of Zn//Cu and 3D-ULPT-Zn//Cu asymmetric cells. Voltage-capacity profiles of (**i**) Zn//Cu, and (**J**) 3D-ULPT-Zn//Cu asymmetric cells

S23, Supporting Information) of the 3D-ULPT-Zn anode after 100 cycles at 15 mA cm^{-2} and 15 mAh cm^{-2} was significantly lower than bare Zn anode, indicating the excellent side reaction resistance of 3DMNs at high current density and areal capacity. Most notably, compared with the work-rest tests (Fig. S24, Supporting Information) of Zn//Zn symmetric batteries (273 h), the stable cycling of the 3D-ULPT-Zn//3D-ULPT-Zn symmetric cell exceeded 1600 h, verifying the durability of 3DMNs in practical applications. Fig. 3(d) evaluates the rate performance of bare Zn and 3D-ULPT-Zn anodes at various current densities and a fixed areal capacity of 1 mAh cm^{-2}. The overpotential of the bare Zn is higher than the 3D-ULPT-Zn anode, particularly at high current density (>5 mA cm^{-2}), where the overpotential continuously increases and fluctuates violently. It could be essentially ascribed to the high interface resistance caused by the constant corrosion and generation of by-products on the bare surface. By contrast, the 3D-ULPT-Zn anode exhibits ultralow overpotential and ultrastable voltage distribution with increasing current density. After returning to the initial current density, the stable operation indicates

that the 3D-ULPT-Zn electrode possesses excellent rate stability. Such a result is consistent with the lower polarization voltage of the 3D-ULPT-Zn anode under different current densities (Fig. 3e). The above results indicate that the 3DMN can provide ultrafast Zn^{2+} transport and reduced local current density to significantly optimize the deposition behavior at high current density/areal capacity.

The ion transport characteristics on different electrodes were revealed through temperature-dependent electrochemical impedance spectroscopy (EIS). Excitingly, it is found that all charge-transfer resistance (R_{ct}) of the 3D-ULPT-Zn symmetric cell is much lower than that of the bare Zn when evolving at different temperatures ranging from 30 to 70 °C (Fig. S25 and Table S1, Supporting Information), signifying a significantly improved charge transfer ability. The activation energy (E_a) required for the electrode interface redox reaction was quantitatively calculated based on the Arrhenius equation [17]. As expected, the computed E_a for 3D-ULPT-Zn is 24.7 kJ mol^{-1}, whilst that for bare Zn is remarkably greater at 33.1 kJ mol^{-1} (Fig. 3f). This result indicates that the 3DMN can significantly improve the redox kinetics at the electrode/electrolyte interface to boost Zn^{2+} transport. Notably, thanks to ultrafast electron transfer and optimized deposition behavior, the 3D-ULPT-Zn anode provides overwhelming advantages over previously reported Zn electrodes with 3D structures (Fig. 3g and Table S2, Supporting Information), indicating the superiority of the one-step ULPT.

Asymmetric cells were utilized to further evaluate the reversibility of Zn plating/stripping performance. As shown in Fig. 3(h), the average CE of the Zn//Cu asymmetric cell is relatively low (~98.72%) at a current density of 10 mA cm^{-2} and an areal capacity of 1 mAh cm^{-2}, which could be attributed to the uncontrolled dendrites and severe interface side reactions. Meanwhile, the voltage plateau of the bare Zn electrode sharply decreased (Fig. 3i) at 807 cycles, indicating the uncontrollable battery failure caused by dendrite growth. However, the 3D-ULPT-Zn//Cu cell operates highly reversible plating/stripping behavior and a remarkable average CE of 99.71% beyond 1700 cycles (Fig. 3j). Furthermore, compared to the bare Zn (150.4 mV), the 3D-ULPT-Zn anode exhibits a smaller voltage gap (83.1 mV) after varied cycles due to the fast Zn^{2+} transport. In addition, the cyclic voltammetry (CV) shows that the 3D-ULPT-Zn//Cu cell has a smaller nucleation overpotential (Fig. S26, Supporting Information), implying higher nucleation kinetics and lower nucleation potential barriers. The voltage-time curves of different electrodes and the flat voltage platform (Fig. S27, Supporting Information) further demonstrate the high stability of the 3D-ULPT-Zn anode.

To reveal the Zn nucleation behavior and demonstrate the zincophilic character, the adsorption and diffusion of Zn^{2+} on Zn(001) and Zn(001)/ZnO(100) surfaces (Fig. 4a-b) were performed using density functional theory (DFT) calculations based on the HRTEM results (Fig. 1j-k). The optimized stable site of Zn^{2+} (Fig. S28, Supporting Information) provides a theoretical foundation for calculations. As shown in Fig. 4(c), the optimized adsorption energies of Zn^{2+} on Zn(001) and Zn(001)/ZnO(100) surfaces are evaluated as -0.25 eV and -1.82 eV, respectively. Compared to the Zn(001) surface, the Zn(001)/ZnO(100) surface exhibits a stronger attraction towards Zn^{2+}. Besides, the Bader charge calculation indicates that the 0.38e transfer between Zn^{2+} and the Zn(001)/ZnO(100) surface is highly larger than that of the Zn(001) surface (0.03e), indicating a stronger interaction between Zn^{2+} and Zn(001)/ZnO(100) system.
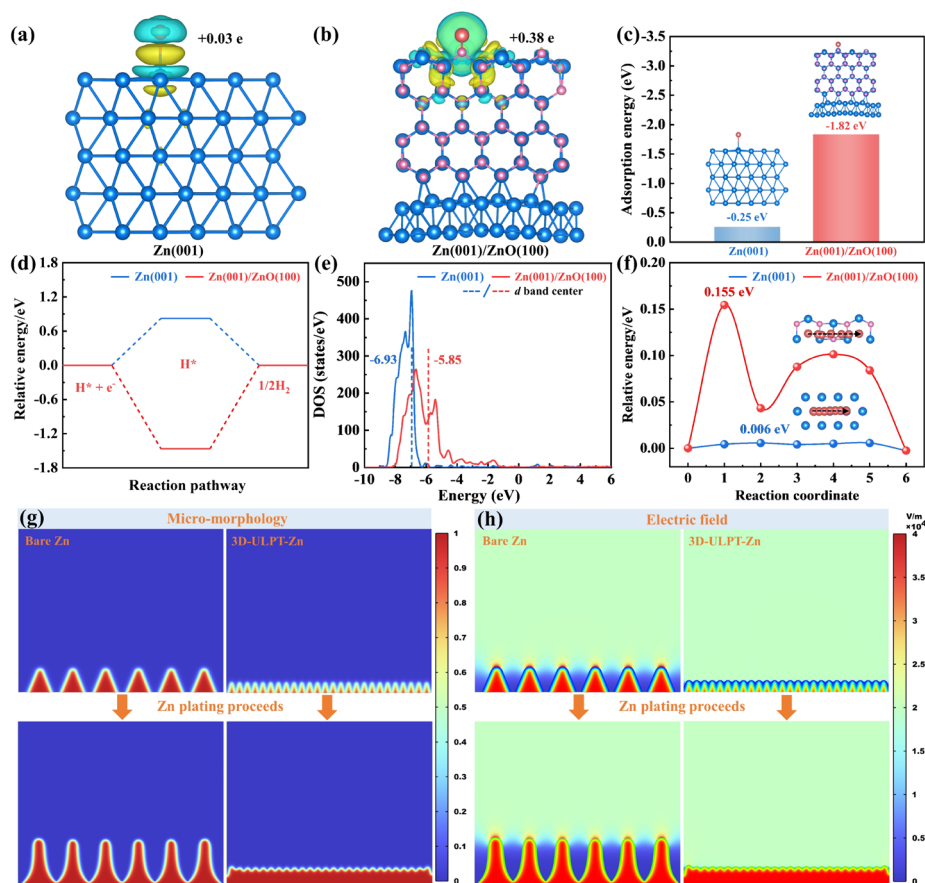
Fig. 4 DFT-calculated charge density differences of (**a**) Zn(001) and (**b**) Zn(001)/ZnO(100) surfaces for Zn^{2+} adsorption. Remarks: Zn (blue), O (pick), and Zn^{2+} (red). Yellow and cyan regions represent the increased and decreased electron density (isosurface value: 0.0003 electron $Bohr^{-3}$). **c** Calculated absorption energy of Zn^{2+} on Zn(001) and Zn(001)/ZnO(100) surfaces. **d** Calculated hydrogen adsorption free energy on Zn(001) and Zn(001)/ZnO(100) surfaces. **e** Density of states (DOS) of Zn(001) and Zn(001)/ZnO(100) surfaces. **f** The activation energy for Zn^{2+} to migrate from one energy minima to another nearby minimum on Zn(001) and Zn(001)/ZnO(100) surfaces. Numerical simulations of (**g**) dendrite growth and (**h**) electric field during the Zn plating process before and after 30 s

Consequently, the Zn^{2+} tends to nucleate on the Zn(001)/ZnO(100) surface instead of on the Zn substrate, which is in agreement with the experimental result (Fig. 2e). The high affinity of 3DMNs promotes the effective nucleation of Zn^{2+} and becomes an ideal "deposition site" to eliminate the dendrites that grow upon Zn anodes. Recent investigations showed that the Zn@ZnO-3D system is able to reduce surface-side reactions and hydrogen evolution [46]. In the present exploration, the HER of Zn(001) and Zn(001)/ZnO(100) surfaces are evaluated, as shown in Fig. 4(d). The ability of hydrogen absorptivity on the Zn(001)/ZnO(100) surface reduces the HER sensitivity, thus allowing more efficient induction of Zn deposition and increasing the HER energy barrier [47, 48]. The *d*-band center (E_d) is commonly employed as a descriptor to evaluate the interaction between the substrate and the adsorbate [49]. As shown in Fig. 4(e), the value of E_d on the Zn(001)/ZnO(100) surface (-5.85 eV) is significantly closer to the Fermi energy level than that of the Zn(001) surface with a value of -6.93 eV, indicating a stronger adsorption ability [50]. Fig. 4(f) displays the diffusion paths of Zn^{2+} on Zn(001) and Zn(001)/

ZnO(100) surfaces. The energy barrier associated with Zn^{2+} diffusion on the Zn(001) surface is 0.006 eV, indicating a transient and rapid diffusion process of Zn^{2+}. Compared to the Zn(001)/ZnO(100) surface, the diffusion resistance of Zn^{2+} is higher (0.155 eV). During the nucleation stage, the low energy barrier inevitably causes the accumulation of Zn^{2+} on Zn nuclei, and the resulting cusp effect can lead to the growth of dendrites [51]. In stronger contrast, the relatively difficult diffusion on the Zn(001)/ZnO(100) surface effectively prevents the migration and aggregation of Zn^{2+}, thus acting as a buffer against dendrite growth [52]. Therefore, the Zn(001)/ZnO(100) surface can effectively capture and fix Zn^{2+} to reduce the interfacial concentration gradient between the electrode and the electrolyte. DFT calculations demonstrate that the higher adsorption energy of the Zn(001)/ZnO(100) layer to Zn^{2+} and the higher diffusion barrier, imparting 3D-ULPT-Zn anode the ability to inhibit dendrite growth and HER.

To further understand the effect of 3DMNs on the Zn deposition mechanisms, the dendrite growth, electric field distribution, and Zn^{2+} concentration distribution between the anode and electrolyte were simulated using COMSOL Multiphysics® software (Fig. S29, Supporting Information). The rough surface causes Zn^{2+} to preferentially deposit at prominent positions and form nucleation hot spots for the bare Zn anode, resulting in a distinct intensity gradient in the electric field distribution (Fig. 4g). The enhanced local electric field and intensity gradient drive more Zn^{2+} adhering to the rough surface to form dendrites (Fig. 4h). These dendrites will increase the thickness of the electrode and may puncture the separator to trigger a short circuit. In particular, the concentration polarization occurs on the bare Zn anode, causing a sharp increase in the Zn^{2+} flux near the protrusion and eventually evolving into irregular deposition (Fig. S30, Supporting Information). As expected, the electric field and Zn^{2+} distribution in the vicinity of the 3D-ULPT-Zn anode are uniform, making the Zn^{2+} preferentially deposit at the zinophilic position on the 3D-ULPT-Zn anode. Consequently, optimized selective behaviors guarantee the effective adsorption of Zn^{2+} to achieve a dendritic-free morphology.

Full cells (note as $Zn//MnO_2@CNT$ and $3D\text{-}ULPT\text{-}Zn//MnO_2@CNT$) were further assembled to evaluate the feasibility of 3D-ULPT-Zn electrodes in practical applications. The XRD pattern and TEM image demonstrate the successful synthesis of $MnO_2@CNT$ cathode materials (Fig. S31, Supporting Information), and the nanostructure ensures fast ion/electron transport. The CV curve (Fig. 5a) reveals bimodal reversible redox reactions between MnO_2 and $MnOOH$ [53]. Notably, the $3D\text{-}ULPT\text{-}Zn//MnO_2@CNT$ full cell exhibits a minor voltage discrepancy between the redox peaks, proving the faster charge transfer rate, which is consistent with the reduced voltage hysteresis of discharge-charge curves (Fig. 5b) and excellent rate performance (Figs. 5c and S32, Supporting Information). The rapid reaction kinetics and low polarization could be mainly ascribed to reduced interface resistance (Fig. 5d) and side reactions inhibited by 3DMNs. Most importantly, the $3D\text{-}ULPT\text{-}Zn//MnO_2@CNT$ full cell maintained high-capacity retention of 71.8% after 1000 cycles at 1 A g^{-1} (Fig. 5e), with a CE of up to 99.8%. In contrast, the $Zn//MnO_2@CNT$ full cell suffered a rapid capacity lessening with a capacity retention of 42.1% under consistent conditions. The postmortem analysis based on SEM images (Fig. S33, Supporting Information) shows that the Zn flakes generated upon the 3D-ULPT-Zn anode are smaller than the bare Zn, indicating more uniform deposition and faster plating/stripping processes. However, the cycled bare Zn anode was covered
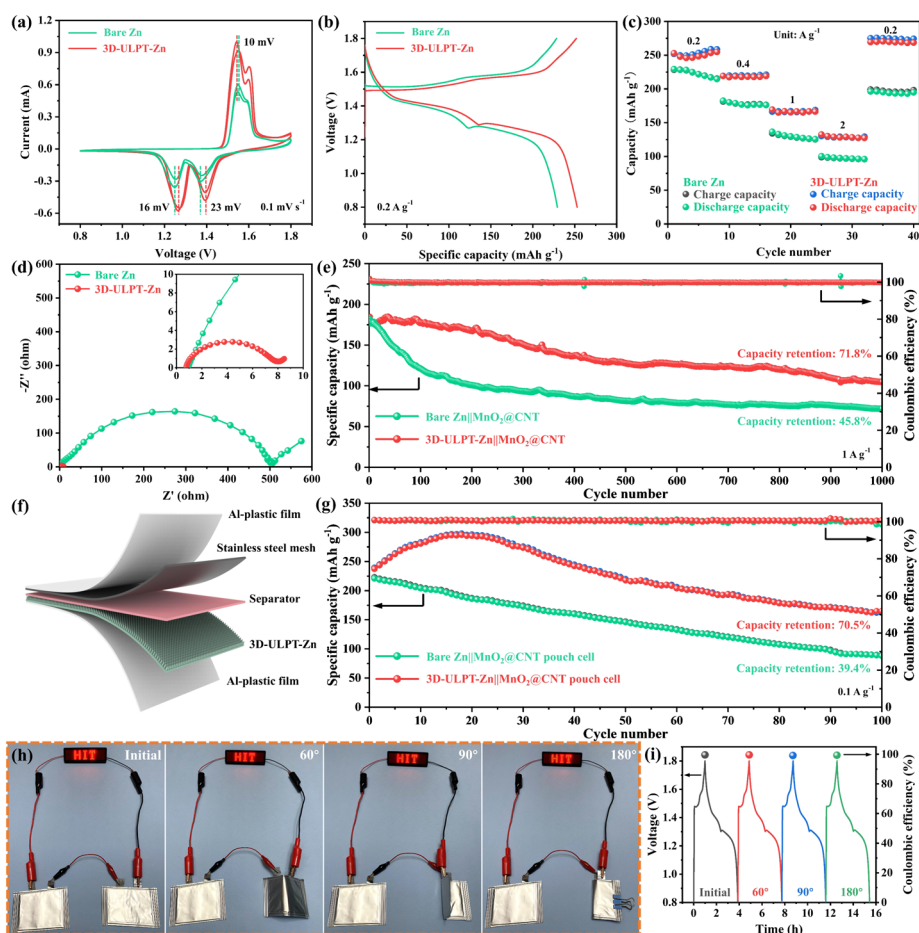
Fig. 5 a CV curves of Zn//MnO$_2$@CNT and 3D-ULPT-Zn//MnO$_2$@CNT full cells at 0.1 mV s^{-1}. **b** The first discharge-charge curves of Zn//MnO$_2$@CNT and 3D-ULPT-Zn//MnO$_2$@CNT full cells at 0.2 A g^{-1}. **c** Rate performance. **d** Initial EIS patterns. **e** Long-term cycle tests of Zn//MnO$_2$@CNT and 3D-ULPT-Zn//MnO$_2$@CNT full cells at 1 A g^{-1}. **f** Schematic diagram of the 3D-ULPT-Zn//MnO$_2$@CNT pouch cell. **g** Long-term cycle tests of Zn//MnO$_2$@CNT and 3D-ULPT-Zn//MnO$_2$@CNT pouch cells at 0.1 A g^{-1}. **h** Digital photographs of 3D-ULPT-Zn//MnO$_2$@CNT pouch cells powering LED lights at different bending states. **i** Voltage profiles and CEs of the 3D-ULPT-Zn//MnO$_2$@CNT pouch cell under different conditions

by a large number of cluttered dendrites and more O and S contents, which is detrimental to maintaining battery capacity. Furthermore, the EIS analysis after 1000 cycles (Fig. S34, Supporting Information) reveals that the 3D-ULPT-Zn//MnO$_2$@CNT full cell has a lower interface resistance throughout the cycling process, which essentially ascribed to the more robust charge transfer improved by the super-hydrophilicity of the 3D-ULPT-Zn anode. Therefore, the enhanced cycling stability and rate performance of the 3D-ULPT-Zn//MnO$_2$@CNT cell demonstrate the practical design of 3DMNs.

The one-step preparation strategy of 3DMNs on Zn anodes can be easily scaled up and prepared in adjustable-size pouch cells. The cycling life of the 3D-ULPT-Zn//3D-ULPT-Zn pouch cell (Fig. S35(a), Supporting Information) reaches 2000 h at 1 mA cm^{-2} and 0.5 mAh cm^{-2} (Fig. S36, Supporting Information) indicates the stability of 3DMNs in large areas applications. Fig. 5(f) shows the schematic diagram of the 3D-ULPT-Zn//MnO$_2$@CNT pouch cell, which contains a 3D-ULPT-Zn anode, MnO$_2$@CNT cathode,

glass fiber separator, and aluminum (Al) plastic film. As a result, the 3D-ULPT-Zn// MnO_2@CNT pouch cell (Fig. S35(b), Supporting Information) provides a high capacity of 300 mAh g^{-1} at 0.1 A g^{-1} and a high-capacity retention rate (70.5%) after 100 cycles (Fig. 5g), significantly higher than the Zn//MnO_2@CNT cell with lower storage (39.4%). Such a result convincingly demonstrates that the 3D-ULPT-Zn electrode prominently inhibits side reactions. Fig. 5(h) shows that the 3D-ULPT-Zn//MnO_2@CNT pouch cell can power LEDs and display "HIT" stably under different bending states. Furthermore, the constant voltage curves, highly stable CEs (Fig. 5i), and discharge-charge curves (Fig. S37, Supporting Information) under different conditions support the excellent flexibility and stability of the 3D-ULPT-Zn anode. It is believed that this one-step prepared 3D-ULPT-Zn anodes is promising in large-scale flexible devices.

Conclusions

In summary, we report a simple and easily scalable method for constructing super hydrophilic and zincophilic 3DMNs to effectively address the issue of zinc anode instability by one-step ULPT. The 3DMNs well integrate low local current density, fast Zn^{2+} transport, and sufficiently high Zn loading space. Benefiting from these synergistic merits, the 3D-ULPT-Zn anode effactually optimized the electric field distribution, Zn^{2+} ion flux, and nucleation behavior, thus achieving homogenous Zn deposition and inhibiting side reactions. In particular, based on comprehensive characterizations and computational simulations coupled with electrochemistry tests, it was verified that the 3DMNs could induce uniform nucleation and eliminate dendrite growth. As a result, the 3D-ULPT-Zn anode possessed overwhelmingly competitive advantages on prolonged cycling lifespans (2530 h at 1 mA cm^{-2}/1 mAh cm^{-2}; 240 h at 15 mA cm^{-2}/15 mAh cm^{-2}) with ultralow overpotential, significantly superior to previously reported Zn anodes with 3D structures. Most importantly, the 3D-ULPT-Zn//MnO_2@CNT full cell and pouch cell highlight enhanced capacity retention than Zn//MnO_2@CNT cells. This work offers a novel and practical approach for constructing 3DMNs on Zn anodes to achieve high-performance AZIBs, which can be extended to become a universal surface modification strategy for other metal electrodes.

Methods

Materials preparation

In this work, the size of the commercial Zn foil is $10 \times 10 \times 0.1$ cm^3. Firstly, the Zn foil was ultrasonically cleaned in ethanol for 15 min to remove surface contaminants. Then, the 3DMNs are scanned in the *x* and *y* directions by the ULPT in the atmospheric environment. The picosecond laser (PX200-3-GF, EdgeWave, Germany) parameters are as follows: the spot diameter is 10 μm, wavelength is 355 nm, and pulse duration is 8 ps. The single processing area of the 3D-ULPT-Zn anode is 15×15 mm^2 and can achieve a maximum area of 200×200 mm^2 through the splicing function, which can meet the preparation of coin and pouch cells with different sizes. The Zn foil was processed with the following parameters: the laser pulse fluence is calculated from $F=2*E/(\pi*R^2)$ and is set to 2 J cm^{-2}, where E is the laser pulse energy and R is the radius of spot. The scanning speed is 1000 mm/s, repetition frequency is 1 MHz, scanning interval is 8 μm, and scanning repetitions (R_s) are various values (1, 5, 10, 20, 30, and 40). Notably, compared

to the mainstream 1030 nm infrared and 515 nm green light wavelengths, the 355 nm ultraviolet wavelength can effectively restrict the thermal effect, which results in high temperature and high pressure being confined to local melting regions. As a result, the suppression of thermal effects resulted in ultrafine and controllable 3DMNs, which improved the electrochemical performance. More importantly, a higher power of picosecond lasers can achieve a higher energy density, demonstrating significant advantages in processing efficiency and quality. Compared with femtosecond lasers, picosecond lasers significantly reduce processing costs and are more suitable for practical productions in energy storage devices to achieve industrialization. Combining the low cost, high efficiency and processing quality of ultrafast laser processing of 3DMNs, a 355 nm ultraviolet wavelength and an 8 ps pulse duration were adopted in this work.

Materials characterization

The microstructure of different Zn anodes was characterized by field emission scanning electron microscopy (SEM, Zeiss Gemini 300, Germany). X-ray diffraction (XRD, Bruker D8, Germany) was used to analyze the phase composition of the electrode. The contact angle goniometer (Dataphysics OCA20) was employed to analyze the surface wettability of different Zn anodes. The change of the cross-section morphology was observed by a high-resolution optical microscope (OM, Metatest corporation, China) with a current density of 10 mA cm^{-2}. 3D images were obtained using a 3D measurement microscope (Micro 1000, China), and the 50X Nikon CF IC Epi Plan DI Mirau (MUL40501, Japan) was selected as the microscope objective with a resolution of 0.5 um. The atomic structure and energy dispersive spectroscopy EDS element distribution of the Zn anode was studied by field emission transmission electron microscopy (TEM, Talos F200S, FEI Corp., USA) with a voltage of 200 kV. The TEM sample was prepared by a focused ion beam milling system (FIB, Helios Nanolab 600i, FEI Corp., USA). The surface of the sample was coated with a Pt layer to avoid Ga ion damage. The mass proportion of active substance of the MnO_2@CNT composite material was obtained through thermogravimetric testing under a temperature range of 25 to 800 °C and a heating rate of 10 °C/min.

Preparation of MnO$_2$@CNT

MnO_2@CNT composites were prepared by a combined chemical vapor deposition-hydrothermal method. Firstly, CNTs were synthesized by the chemical vapor deposition method with ethanol as the carbon precursor. In this work, nickel (Ni) nanoparticles were used as the catalysts for preparing CNTs. The Ni catalysts were prepared by mixing 0.1 M $Ni(NO_3)_2$ and 0.2 M NaOH to obtain precipitation, which was annealed at 400 °C for 2 h in Ar+5% H_2 to synthesize Ni catalysts. Then, the Ni catalysts were put into a tube furnace and treated at 700 °C under a mixed-gas atmosphere of 200 sccm Ar+20 sccm H_2 for 1 h. Then the Ar+H_2 gas saturated with ethanol was introduced in the furnace for 2 h. Finally, the samples were immersed into a solution with 1M HCl and 1M $FeCl_3$ at 85 °C for 12 h to remove the Ni catalyst to obtain CNTs.

Afterward, MnO_2 was assembled on the CNTs by a facile hydrothermal method. The hydrothermal reaction solution consisted of 0.5 M $KMnO_4$. The CNTs were immersed

into the above solution, and the autoclaves were kept at 160 °C for 2 h. Finally, the samples were rinsed with deionized water and ethanol to form MnO_2@CNT composites.

Electrochemical measurements

The symmetrical coin battery (CR2025) was assembled using Zn or 3D-ULPT-Zn foils (ϕ12 mm) and glass fiber membrane (Whatman, GF/D, ϕ16 mm) as the separator. The Coulombic efficiency measurement was tested by asymmetric cells. Zn/3D-ULPT-Zn and Cu foils (ϕ12 mm) were used as the working and counter electrodes, whereas the 2 M $ZnSO_4$ aqueous solution was used as electrolytes in both symmetric and asymmetric cells. The MnO_2@CNT cathode was prepared using synthesized material (MnO_2@CNT), acetylene black, and polyvinylidene fluoride in a weight ratio of 7: 2: 1 through a slurry coating method on the stainless-steel mesh (ϕ10 mm). After maintaining at 60 °C for 24 h, the active material with a mass loading of 1.2 mg cm^{-2} was obtained. The 2 M $ZnSO_4$+0.2 M $MnSO_4$ aqueous solution was used in full cells as the electrolyte. The CV measurement was performed on the electrochemical workstation (Chenhua, China). LSV and *i-t* tests are carried out in a three-electrode configuration using bare Zn or 3D-ULPT-Zn anodes as working electrodes, a platinum plate as the counter electrode, and an Ag/AgCl electrode as the reference electrode. The 2 M $ZnSO_4$ aqueous electrolyte solution was used in the *i-t* test. In contrast, the 1 M Na_2SO_4 aqueous electrolyte was used in the LSV test to exclude the influence of competitive galvanizing processes in Zn salts. The EIS were collected on the PAR2273 electrochemical workstation, with a frequency range from 1 MHz to 0.01 Hz. The NEWARE Battery Test System (CT-4008Tn, Shenzhen, China) was used to test the GCD performance of the two systems. The stripping cutoff voltage of asymmetric cells is set to 1 V (vs. Zn^{2+}/Zn). The cutoff voltage of the full cells is in the range of 0.8 to 1.8 V. The data recording time of the cell is set to 30 s and the cell test protection voltage range is -3 V to 3 V. The electrode after cycling was removed from the CR2025 battery and cleaned with a large amount of deionized water to remove the attached salt. The LED display was obtained from Canrd.

Finite element analysis method

In the present work, appropriate 2D geometric models are established to simulate the bare Zn and 3D-ULPT-Zn anodes during the plating process. The field finite element method using COMSOL Multiphysics® software was implemented to examine the electric field distribution, Zn^{2+} concentration distribution, and dendrite growth during the Zn plating process. The electric field module calculates the electric field distribution in real-time. The Fick diffusion mass transfer is controlled by the Nernst-Planck equation and coupled with the current. The Level Set interface capture diffusion prevents the dendrite formation caused by electrodeposition in practical applications. The Level Set variable is replaced by the velocity field (v_x and v_y), which is determined by the diffusion flux of Zn^{2+}. Therefore, finite element simulations are conducted based on the following coupled equations (1, 2, 3, 4 and 5).

$$\mathbf{E} = -\nabla V$$

(1)

$$\mathbf{J} = -D\nabla c - zuFc\nabla V \tag{2}$$

$$\frac{\partial c}{\partial t} + \nabla \cdot (-D\nabla c) = 0 \tag{3}$$

$$v_x = -D\frac{\partial c}{\partial_x} \times \frac{2M_{\mathrm{Zn}}}{\rho_{\mathrm{Zn}}} \tag{4}$$

$$v_y = -D\frac{\partial c}{\partial_y} \times \frac{2M_{\mathrm{Zn}}}{\rho_{\mathrm{Zn}}} \tag{5}$$

where $\mathbf{E}$ is the electric field, V is the electric potential, and $\mathbf{J}$ is the molar flux relative to the convective transport. The parameters D, c, and z represent the diffusion coefficient, concentration field, and chemical valence of Zn^{2+}, respectively. u is the Mobility of Zn^{2+}, F is the Faraday constant, t is diffusion time, and M_{Zn} and ρ_{Zn} in order denote the molar mass and density of Zn.

DFT calculations

The first-principle calculation based on the DFT is adopted to study the structure-activity relationship of Zn anodes at the atomic scale. The spin-polarized analyses were performed via the plane-wave projector augmented-wave method [54], applying the semi-local Perdew-Burke-Ernzerhof exchange-correlation functional [55], as implemented in the Vienna *ab* initio simulation package (VASP) code [56]. A plane-wave cutoff energy of 400 eV was used. Brillouin-zone integration was performed on gamma-centered symmetry-reduced meshes. The Brillouin zone is sampled with Gama-centered 1x1x1 *k*-point meshes for surface calculations [57]. The structures were first relaxed with the implemented conjugate-gradient algorithm until the convergence tolerance of Hellmann-Feynman forces and energy on each atom was less than 0.05 eV/Å and 10^{-4} eV/atom, respectively. In addition, transition states were searched by the climbing image nudged-elastic-band method combined with VTST code [58, 59]. The adsorption energy (E_{ads}) of each elementary step was calculated via the following equation (6):

$$E_{ads} = E_{\mathrm{total}} - E_{slab} - E_{\mathrm{Zn}} \tag{6}$$

where E_{total} and E_{slab} are the total energy with and without Zn atom adsorption, respectively, and E_{Zn} is the atomic energy of Zn.

Abbreviations

AZIBs	Aqueous zinc-ion batteries
CV	Cyclic voltammetry
DOS	Density of states
DFT	Density functional theory
EDS	Energy dispersive spectroscopy
EIS	Impedance spectroscopy
FIB	Focused ion beam
GCD	Galvanostatic charge-discharge
HRTEM	High-resolution transmission electron microscopy
HAADF	High angle annular darkfield
HER	Hydrogen evolution reaction
LSV	Linear scanning voltammetry

SEM	Scanning electron microscope
SAED	Selected area electron diffraction
3DMNs	Three-dimensional micro-/nanostructures
ULPT	Ultrafast laser processing technology
XRD	X-ray diffraction

Supplementary Information

The online version contains supplementary material available at https://doi.org/10.1186/s43074-024-00122-x.

> **Supplementary Material 1.**

Availability of data and materials
The data that support the findings of this study are available from the corresponding author on reasonable request.

Declarations

Ethics approval and consent to participate
There is no ethics issue for this paper.

Competing interests
The authors declare that they have no conflict of interests.

References
1.   Han D, Wang Z, Lu H, Li H, Cui C, Zhang Z, Sun R, Geng C, Liang Q, Guo X, Mo Y, Zhi X, Kang F, Weng Z, Yang Q-H. A self-regulated interface toward highly reversible aqueous zinc batteries. Adv Energy Mater. 2022;12:2102982.
2.   Gao Y, Yan Z, Gray J, He X, Wang D, Chen T, Huang Q, Li Y, Wang H, Kim S, Mallouk T, Wang D. Polymer-inorganic solid-electrolyte interphase for stable lithium metal batteries under lean electrolyte conditions. Nat Mater. 2019;18:384–9.
3.   Fang G, Zhou J, Pan A, Liang S. Recent advances in aqueous zinc-ion batteries. ACS Energy Lett. 2018;3:2480–501.
4.   Zhao C-X, Chen W-J, Zhao M, Song Y-W, Liu J-N, Li B-Q, Yuan T, Chen C-M, Zhang Q, Huang J-Q. Redox mediator assists electron transfer in lithium–sulfur batteries with sulfurized polyacrylonitrile cathodes. EcoMat. 2021;3:e12066.
5.   Yu H, Zeng Y, Li N, Luan D, Yu L, Lou X. Confining Sn nanoparticles in interconnected N-doped hollow carbon spheres as hierarchical zincophilic fibers for dendrite-free Zn metal anodes. Sci Adv. 2022;8:eabm5766.
6.   Yin Y-C, Yang J-T, Luo J-D, Lu G-X, Huang Z, Wang J-P, Li P, Li F, Wu Y-C, Tian T, Meng Y-F, Mo H-S, Song Y-H, Yang J-N, Feng L-Z, Ma T, Wen W, Gong K, Wang L-J, Ju H-X, Xiao Y, Li Z, Tao X, Yao H-B. A LaCl$_3$-based lithium superionic conductor compatible with lithium metal. Nature. 2023;616:77–83.
7.   Wang F, Zhang J, Lu H, Zhu H, Chen Z, Wang L, Yu J, You C, Li W, Song J, Weng Z, Yang C, Yang Q-H. Production of gas-releasing electrolyte-replenishing Ah-scale zinc metal pouch cells with aqueous gel electrolyte. Nat Commun. 2023;14:4211.
8.   Xie C, Li Y, Wang Q, Sun D, Tang Y, Wang H. Issues and solutions toward zinc anode in aqueous zinc-ion batteries: a mini review. Carbon Energy. 2020;2:1–21.
9.   Li C, Xie X, Liang S, Zhou J. Issues and future perspective on zinc metal anode for rechargeable aqueous zinc-ion batteries. Energy Environ Mater. 2020;35:19–46.
10. Liu B, Wei C, Zhu Z, Fang Y, Bian Z, Lei X, Zhou Y, Tang C, Qian Y. Regulating Surface Reaction Kinetics through Ligand Field Effects for Fast and Reversible Aqueous Zinc Batteries. Angew Chem Int Ed. 2022;61:e202212780.
11. Lv Y, Zhao M, Du Y, Kang Y, Xiao Y, Chen S. Engineering self-adaptive electric double layer on both electrodes for high-performance zinc metal batteries. Energy Environ Sci. 2022;5:4748–60.
12. Ren H, Li S, Wang B, Zhang Y, Wang T, Lv Q, Zhang X, Wang L, Han X, Jin F, Bao C, Yan P, Zhang N, Wang D, Cheng T, Liu H-K, Dou S. Molecular crowding effect mimicking cold resistant plant to stabilize zinc anode with wider service temperature range. Adv Mater. 2022;35:2208237.

13. Kwon M, Lee J, Ko S, Lim G, Yu S-H, Hong J, Lee M. timulating Cu-Zn Alloying for Compact Zn Metal Growth towards High Energy Aqueous Batteries and Hybrid Supercapacitors. Energy Environ Sci. 2022;15:2889–99.
14. Tian H, Feng G, Qi W, Li Z, Zhang W, Lucero M, Feng Z, Wang Z, Zhang Y, Zhen C, Gu M, Shan X, Yang Y. Three-dimensional Zn-based alloys for dendrite-free aqueous Zn battery in dual-cation electrolytes. Nat Commun. 2022;13:7922.
15. Meng H, Ran Q, Dai T, Shi H, Zeng S, Zhu Y, Wen Z, Zhang W, Lang X, Zheng W, Jiang Q. Surface-alloyed nanoporous zinc as reversible and stable anodes for high-performance aqueous zinc-ion battery. Nano-Micro Lett. 2022;14:128.
16. Gan H, Wu J, Li R, Huang B, Liu H. Ultra-stable and deeply rechargeable zinc metal anode enabled by a multifunctional protective layer. Energy Storage Mater. 2022;47:602–10.
17. Zhao Z, Wang R, Peng C, Chen W, Wu T, Hu B, Weng W, Yao Y, Zeng J, Chen Z, Liu P, Liu Y, Li G, Guo J, Lu H, Guo Z. Horizontally arranged zinc platelet electrodeposits modulated by fluorinated covalent organic framework film for high-rate and durable aqueous zinc ion batteries. Nat Commun. 2021;12:6606.
18. Wang X, Meng J, Lin X, Yang Y, Shuang Z, Yaping W, Pan A. Stable zinc metal anodes with textured crystal faces and functional zinc compound coatings. Adv Funct Mater. 2021;31:2106114.
19. Zhang Z, Yang X, Li P, Wang Y, Zhao X, Safaei J, Tian H, Zhou D, Li B, Kang F, Wang G. Biomimetic dendrite-free multivalent metal batteries. Adv Mater. 2022;34:2206970.
20. Sun PX, Cao Z, Zeng YX, Xie WW, Li NW, Luan D, Yang S, Yu L, Lou XW. High Zinc Utilization Aqueous Zinc Ion Batteries Enabled by 3D Printed Graphene Arrays. Angew Chem Int Ed. 2022;61:e202115649.
21. Ruan J, Ma D, Ouyang K, Shen S, Yang M, Wang Y, Zhao J, Mi H, Zhang P. 3D artificial array interface engineering enabling dendrite-free stable ZN metal anode. Nano-Micro Lett. 2023;15:37.
22. Kim J, Liu G, Shim G, Kim H, Lee J. Functionalized Zn@ZnO hexagonal pyramid array for dendrite-free and ultrastable zinc metal anodes. Adv Funct Mater. 2020;30:2004210.
23. Guo N, Huo W, Dong X, Zhefei S, Lu Y, Wu X, Dai L, Wang L, Lin H, Liu H, Liang H, He Z, Zhang Q. A review on 3D zinc anodes for zinc ion batteries. Small Methods. 2022;6:2200597.
24. Zheng J, Wu Y, Xie H, Zeng Y, Liu W, Gandi A, Zheng Q, Wang Z, Liang H. In situ alloying sites anchored on an amorphous aluminum nitride matrix for crystallographic reorientation of zinc deposits. ACS Nano. 2022;17:337–45.
25. Zhang Z, Said S, Smith K, Zhang Y, He G, Jervis R, Shearing P, Miller T, Brett DJL. Dendrite suppression by anode polishing in zinc-ion batteries. J Mater Chem A. 2021;9:15355–62.
26. Huang Z, Li H, Yang Z, Wang H, Ding J, Xu L, Tian Y, Mitlin D, Ding J, Hu W. Nanosecond laser lithography enables concave-convex zinc metal battery anodes with ultrahigh areal capacity. Energy Storage Mater. 2022;51:273–85.
27. Yang J, Li J, Zhao J, Liu K, Yang P, Fan H. Stable zinc anode enabled by zincophilic polyanionic hydrogel layer. Adv Mater. 2022;34:2202382.
28. Tan D, Sharafudeen KN, Yue Y, Qiu J. Femtosecond laser induced phenomena in transparent solid materials: Fundamentals and applications. Prog Mater Sci. 2016;76:154–228.
29. Zhang B, Wang Z, Tan D, Qiu J. Ultrafast laser-induced self-organized nanostructuring in transparent dielectrics: fundamentals and applications. PhotoniX. 2023;4:24.
30. Chen F, Qing Y, Jiang Z, Hou X. A review of femtosecond-laser-induced underwater superoleophobic surfaces. Adv Mater Interfaces. 2018;5:1701370.
31. Oh H, Lee J, Seo M, Baek I, Byun J, Lee M. Laser-induced dewetting of metal thin films for template-free plasmonic color printing. ACS Appl Mater Interfaces. 2018;10:38368–75.
32. Du L, Yin J, Zeng W, Pang S, Yi H. Fabrication of micro-nano structure Se-doped silicon via picosecond laser irradiation assisted by dopant film. Mater Lett. 2022;331:133463.
33. Liu Y, Ding Y, Xie J, Xu L, WhaJeong I, Yang L. One-Step Femtosecond Laser Irradiation of Single-Crystal Silicon: Evolution of Micro-Nano Structures and Damage Investigation. Mater Des. 2023;225:111443.
34. Yu Y, Zhou L, Cai Z, Luo S, Pan X, Zhou J, He W. Research on the mechanism of DD6 single crystal superalloy wear resistance improvement by femtosecond laser modification. Appl Surf Sci. 2021;577:151691.
35. Jin X, Song L, Dai C, Xiao Y, Han Y, Li X, Wang Y, Zhang J, Zhao Y, Zhang Z, Chen N, Jiang L, Qu L. A flexible aqueous zinc-iodine micro-battery with unprecedented energy density. Adv Mater. 2022;34:2109450.
36. Wang Y, Zhao Z, Zhong J, Wang T, Wang L, Xu H, Cao J, Li J, Zhang G, Fei H, Zhu J. Hierarchically micro/nanostructured current collectors induced by ultrafast femtosecond laser strategy for high-performance lithium-ion batteries. Energy Environ Mater. 2021;5:969–76.
37. Li Q, Wang Q, Li L, Yang L, Wang Y, Wang X, Fang H. Femtosecond laser-etched mxene microsupercapacitors with double-side configuration via arbitrary on- and through-substrate connections. Adv Energy Mater. 2020;10:2000470.
38. Liu H, Yixin Z, Moon K, Chen Y, Shi D, Chen X, Wong C. Ambient-air in situ fabrication of high-surface-area, superhydrophilic, and microporous few-layer activated graphene films by ultrafast ultraviolet laser for enhanced energy storage. Nano Energy. 2021;94:106902.
39. Yuan Y, Jiang L, Li X, Zuo P, Xu C, Tian M, Zhang X, Wang S, Lu B, Shao C, Zhao B, Zhang J, Qu L, Cui T. Laser photonic-reduction stamping for graphene-based micro-supercapacitors ultrafast fabrication. Nat Commun. 2020;11:6185.
40. Yuan Y, Jiang L, Li X, Zuo P, Zhang X, Lian Y, Ma Y, Liang M, Zhao Y, Qu L. Ultrafast shaped laser induced synthesis of mxene quantum dots/graphene for transparent supercapacitors. Adv Mater. 2022;34:2110013.
41. Yan J, Deng S, Zhu D, Bai H, Zhu H. Self-powered SnSe photodetectors fabricated by ultrafast laser. Nano Energy. 2022;97:107188.
42. Chen J, Qiao X, Han X, Zhang J, Wu H, He Q, Chen Z, Shi L, Wang Y, Xie Y, Ma Y, Zhao J. Releasing plating-induced stress for highly reversible aqueous Zn metal anodes. Nano Energy. 2022;103:107814.
43. Cao Q, Pan Z, Gao Y, Pu J, Fu G, Cheng G, Guan C. Stable Imprinted Zincophilic Zn Anodes with High Capacity. Adv Funct Mater. 2022;32:2205771.
44. Tang B, Shan L, Liang S, Zhou J. Issues and opportunities facing aqueous zinc-ion batteries. Energy Environ Sci. 2019;12:3288–304.
45. Li Q, Chen A, Wang D, Pei Z, Zhi C. "Soft Shorts" hidden in zinc metal anode research. Joule. 2022;6:273–9.
46. Xie X, Liang S, Gao J, Guo S, Guo J, Wang C, Xu G, Wu X, Chen G, Zhou J. Manipulating the ion-transference kinetics and interface stability for high-performance zinc metal anode. Energy Environ Sci. 2020;13:503–10.

47. Seh ZW, Kibsgaard J, Dickens CF, Chorkendorff I, Nørskov JK, Jaramillo TF. Combining theory and experiment in electrocatalysis: Insights into materials design. Science. 2017;355:4998.

48. Laursen A, Varela A, Dionigi F, Fanchiu H, Miller C, Trinhammer O, Rossmeisl J, Dahl S. Electrochemical hydrogen evolution: Sabatier's principle and the volcano plot. J Chem Educ. 2012;89:1595–9.

49. Hammer B, Nørskov J. Theoretical surface science and catalysis-calculations and concepts. Adv Catal. 2000;45:71–129.

50. Zhou J, Han Z, Wang X, Gai H, Chen Z, Guo T, Hou X, Xu L, Hu X, Huang M, Levchenko S. Discovery of quantitative electronic structure-OER activity relationship in metal-organic framework electrocatalysts using an integrated theoretical-experimental approach. Adv Funct Mater. 2021;31:2102066.

51. Liu X, Yang F, Xu W, Zeng Y, He J, Lu X. Zeolitic imidazolate frameworks as Zn^{2+} modulation layers to enable dendrite-free zn anodes. Adv Sci. 2020;7:2002173.

52. M. Kim, Deepika, S. Lee, M. Kim, J. Ryu, K. Lee, L. Archer, W. Cho. Enabling reversible redox reactions in electrochemical cells using protected LiAl intermetallics as lithium metal anodes. Sci Adv. 2019;5:5587.

53. Pan H, Shao Y, Yan P, Cheng Y, Han KS, Nie Z, Wang C, Yang J, Li X, Bhattacharya P, Mueller K, Liu J. Reversible aqueous zinc/manganese oxide energy storage from conversion reactions. Nat Energy. 2016;1:16039.

54. Mortensen J, Hansen L, Jacobsen K. A real-space grid implementation of the Projector Augmented Wave method. Phys Rev B. 2004;71:035109.

55. Perdew J, Burke K, Ernzerhof M. Generalized gradient approximation made simple. Phys Rev Lett. 1996;77:3865–8.

56. Grimme S. Semiempirical GGA-type density functional constructed with a long-range dispersion correction. J Comput Chem. 2006;27:1787–99.

57. Chadi J. Special points for Brillouin-zone integrations. Phys Rev B. 1977;16:1746.

58. Jonsson H. A dimer method for finding saddle points on high dimensional potential surfaces using only first derivatives. J Chem Phys. 1999;111:7010–22.

59. Uberuaga B, Jonsson H. A climbing image nudged elastic band method for finding saddle points and minimum energy paths. J Chem Phys. 2000;113:9901–4.

Publisher's Note

Springer Nature remains neutral with regard to jurisdictional claims in published maps and institutional affiliations.